Analytical solutions for diffuse fluorescence spectroscopy/imaging in biological tissues. Part II: comparison and validation

Kalyan Ram Ayyalasomayajula and Phaneendra K. Yalavarthy*

Supercomputer Education and Research Centre, Indian Institute of Science, Bangalore 560 012, India
**Corresponding author: phani@serc.iisc.in.*

Received December 11, 2012; accepted January 13, 2013;
posted January 16, 2013 (Doc. ID 181539); published February 28, 2013

The analytical solutions for the coupled diffusion equations that are encountered in diffuse fluorescence spectroscopy/imaging for regular geometries were compared with the well-established numerical models, which are based on the finite element method. Comparison among the analytical solutions obtained using zero boundary conditions and extrapolated boundary conditions (EBCs) was also performed. The results reveal that the analytical solutions are in close agreement with the numerical solutions, and solutions obtained using EBCs are more accurate in obtaining the mean time of flight data compared to their counterpart. The analytical solutions were also shown to be capable of providing bulk optical properties through a numerical experiment using a realistic breast model.

OCIS codes: 170.0170, 170.6280, 300.2530, 000.3860.

1. INTRODUCTION

In first part of this work [1], we have developed analytical solutions for the coupled diffusion equations of diffuse fluorescence spectroscopy/imaging of biological tissues in regular geometries using Green's function approach. These regular geometries include infinite, semi-infinite space, infinite slab, circle, finite/infinite cylinder, and sphere. Both zero and extrapolated boundary conditions (EBCs) were deployed to arrive at the analytical solutions for various regular geometries. The expressions for the derived quantities, such as integrated intensity and mean time of flight (MTOF), from these analytical solutions were also provided in the companion paper [1].

In this part, validation of these analytical expressions for regular geometries was performed through comparison with the solutions obtained using established numerical models [2]. Moreover, a comparison of solutions using zero boundary conditions (ZBCs) and EBCs was also included to know the effect of boundary conditions on the accuracy of the derived solutions. Note that in earlier works [3,4], this validation has been achieved through Monte Carlo Simulation, which is equivalent of solving Radiative Transfer Equation. As the analytical solutions are derived for a diffusion equation, the equivalent of solving it through established finite element solution is taken up in this work. The numerical solutions were obtained using NIRFAST Package [2], which is an established numerical model that uses finite element method (FEM) for diffuse fluorescence spectroscopy/imaging. The FEM has the ability to handle irregular geometries and provide more stable solutions compared to other numerical models [2].

As earlier part [1] derived generic closed form solution for any given regular geometry, the derivation of the solution for the regular geometry that is not discussed in part I [1] can be easily written. One such example involving cube geometry is extensively discussed here. The other aspect that has been considered in this part of the work is the usage of analytical expressions in terms of providing bulk fluorescence properties, such as lifetime, for the measurements made on realistic tissues, breast being an example.

Initially we consider solutions obtained using ZBCs and compare them with numerical solutions that are obtained in the frequency domain for both reflectance and transmittance source/detector arrangement. Later we compare the solutions obtained using ZBCs and EBCs with the numerical results compiled for time-domain case to prove that EBC solutions are more accurate compared to their counterpart. Finally, a real breast mesh that had typical three regions of breast, namely adipose, fibroglandular, and tumor, has been utilized to numerically generate the data with different lifetime values for each region. Using this data, the bulk lifetime values have been estimated using the analytical solutions to show the utility in real-time.

2. COMPARISON OF ANALYTICAL AND NUMERICAL SOLUTIONS FOR THE FREQUENCY DOMAIN CASE

For simplicity, initially analytical solutions using ZBC in the frequency domain case was compared with the numerical solutions obtained using FEM. The geometry of the infinite slab was approximated to a finite slab with length (l) and breadth (b) being larger compared to thickness (t). The exact specifications of the finite element meshes considered are provided in Table 1, for the relevant geometries shown in Fig. 1. The optical properties that are used in both analytical and numerical values are given in Table 2. The numerical solutions were computed with utilization of Robin-type (Type-III) boundary conditions, which accommodate the refractive index mismatch at the tissue boundary [2]. The comparison of the magnitude and phase plots of the photon densities for the

Table 1. Specification of the Finite Element Meshes that were Used in this Work[a]

Geometry	Dimensions (mm)	Nodal Distance (mm)	No. of Nodes	No. of Elements	Source Position
Infinite slab	$l = 130$, $b = 130$, $t = 30$	~2	24,505	114,335	(0, 0, 15.0)
Circle	$r = 40$	~0.4	31,780	62,929	(40.0, 0)
Cylinder	$r = 40$, $h = 60$	~3	12,695	63,810	(41.2, −8.2, 0)
Sphere	$r = 40$	~2	20,817	109,335	(41.2, −8.2, 0)
Cube	$a = 40$	~2	39,968	204,993	(0, 0, −49.0)
Breast	—	~4	20,800	109,115	(18.2, −49.1, 37.5)

[a]The appropriate geometries were given in Fig. 1 (slab, circle, sphere, and cylinder) and Fig. 5 (cube and breast), later in the paper.

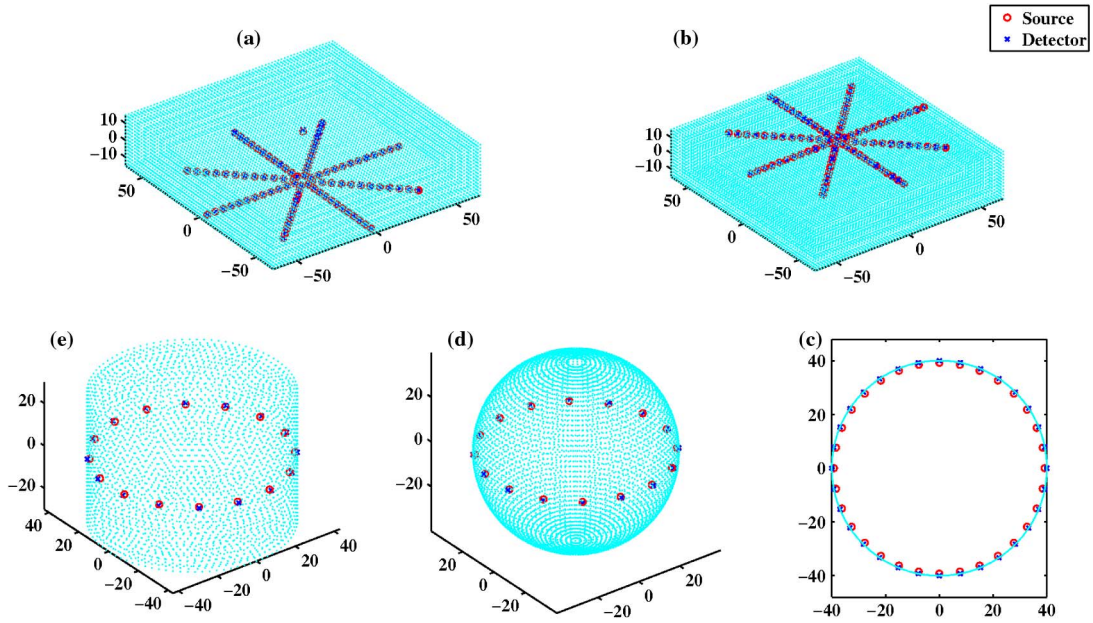

Fig. 1. (Color online) Geometries indicating the source detectors arrangement used in the numerical models. (a) Slab (transmittance), (b) slab (reflectance), (c) circle, (d) sphere, and (e) cylinder.

geometries discussed in part I [1] subjected to ZBC are given in Fig. 2, with operating frequency fixed at 100 MHz. A quantitative comparison of solutions via plot of the error percentage (taking numerical solution as reference) is given in Figs. 3(a) and 3(b) for logarithm of the amplitude and phase, respectively. The solutions (Fig. 2) show that both numerical and analytical models with in-close agreement (average error being around 10%).

The magnitude and phase plots of the photon densities when subjected to EBC for infinite slab geometry are shown in Figs. 3(c) and 3(d). A close comparison of results between ZBC [Figs. 2(a) and 2(b)] and EBC [Figs. 3(c) and 3(d)] show that the difference in logarithm of amplitude data is less than 1% and phase has a difference of less than 4 deg (reflectance case), asserting that usage of EBC for the frequency-domain case may not yield more accurate results when compared to the ones obtained using ZBC. In addition, the computing of solutions that use EBC involves more computational complexity as the terms involved in infinite summations in the expressions of the Green's function require significantly more terms to be included for the Bessel functions to settle.

Table 2. Optical Property Values for all Cases that were Discussed in this Work

Parameter	Values
μ_{ax}	0.0090 mm^{-1}
μ_{am}	0.0060 mm^{-1}
μ_{sx}	1.3140 mm^{-1}
μ_{sm}	1.2730 mm^{-1}
τ	0.1 ns
$\eta\mu_{afl}$	5.0×10^{-10}

3. COMPARISON OF ANALYTICAL AND NUMERICAL SOLUTIONS FOR THE TIME DOMAIN CASE

As the amplitude data is equivalent of the time domain integrated intensity, the same trend of matching values of EBC and ZBC with numerical solutions was observed as earlier. Thus, this comparison was not taken up in this case. The MTOF was considered as the data type for comparison and validation of analytical models. Tables 8–10 of part I [1] gives the analytical solutions. The temporal point spread function (TPSF) of a given mesh geometry can be time resolved over a given time interval in NIRFAST. This capability helps us to determine the MTOF for a source detector pair in the given distribution. The peak value of TPSF measured over the time duration gives the MTOF. The MTOF of analytical and the FEM solutions have been compared using the same values

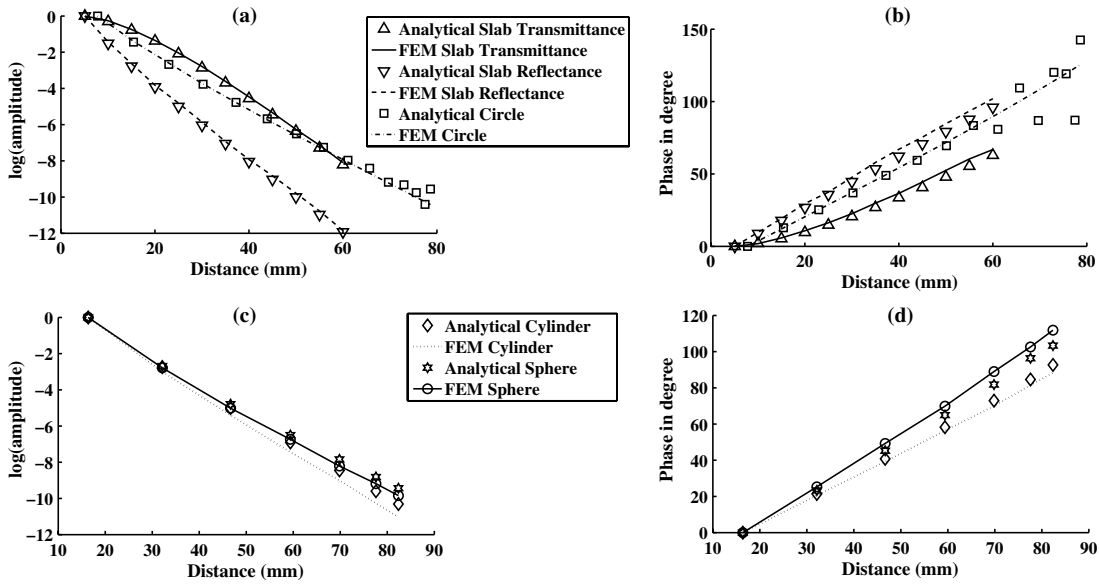

Fig. 2. Comparison of numerical (FEM) and analytical solutions subjected to ZBC for the geometries shown in Fig. 1. (a) and (c) Give the logarithm of amplitude. (b) and (d) Shows comparison of computed phase as a function of source/detector distance.

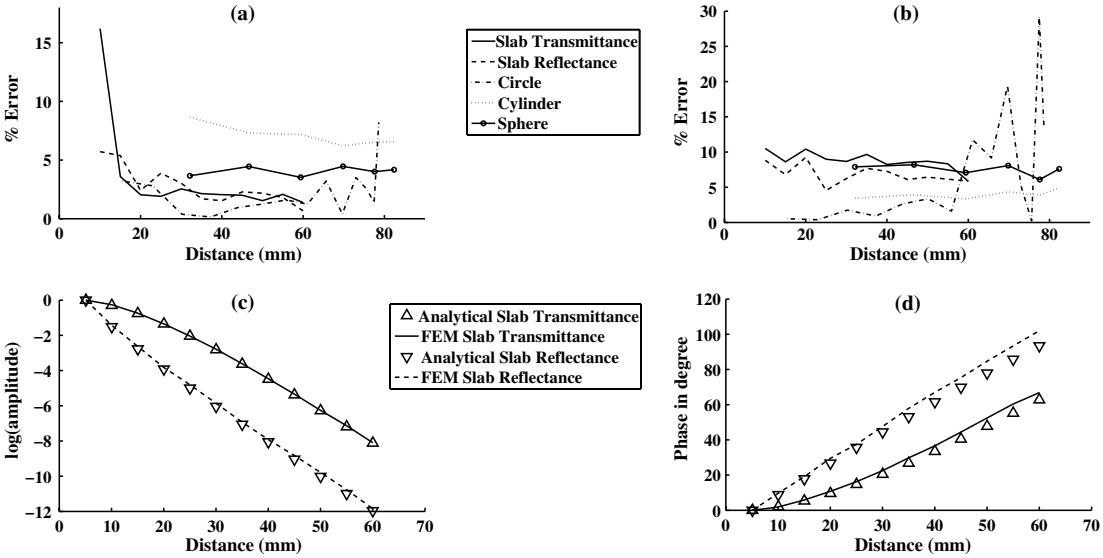

Fig. 3. (a) Shows % difference (or error) between numerical and analytical solutions given in Figs. 2(a) and 2(c) for the case of amplitude data. (b) Same effort as (a) except for phase data. (c) and (d) Same effort as Figs. 2(a) and 2(b) except the boundary condition is changed to EBC for the case of infinite slab [Figs. 1(a) and 1(b)].

as given in Table 2 are given in Fig. 4. The analytical solutions obtained using ZBC are given in Figs. 4(a) and 4(c); corresponding EBC solutions are in Figs. 4(b) and 4(d). It can be easily observed that the analytical solutions that were obtained using EBC are in close agreement with FEM solution, especially near the source (source-detector distance being less than 40 mm) for circle and cylinder. Note that there is lot of ringing for the EBC at far away source/detector locations for the circle case, as the modified Bessel's functions require infinite summation (here used only 130 terms) to have more accuracy, which is not possible in computation. The discrepancy near the source for the infinite slab cases, especially in the reflectance case, is due to source term modeling, where the diffusion equation is not valid. Specifically, the diffusion equation assumes that the source is isotropic, which is only true when the detector is far away from the source (atleast 10 μ_s' with reduced scattering coefficient represented by μ_s') [5].

For all cases considered here, the computation was performed on a workstation with an Intel Xeon 5410 Dual Quad-core processor 2.33 GHz having 64 GB memory. The comparison of computation time among the analytical and numerical models for the geometries considered are given in Table 3. This table also shows that analytical solutions are highly efficient compared to the numerical solutions. The computational complexity of solutions obtained using EBC is higher compared to its counterpart solutions (obtained using ZBC).

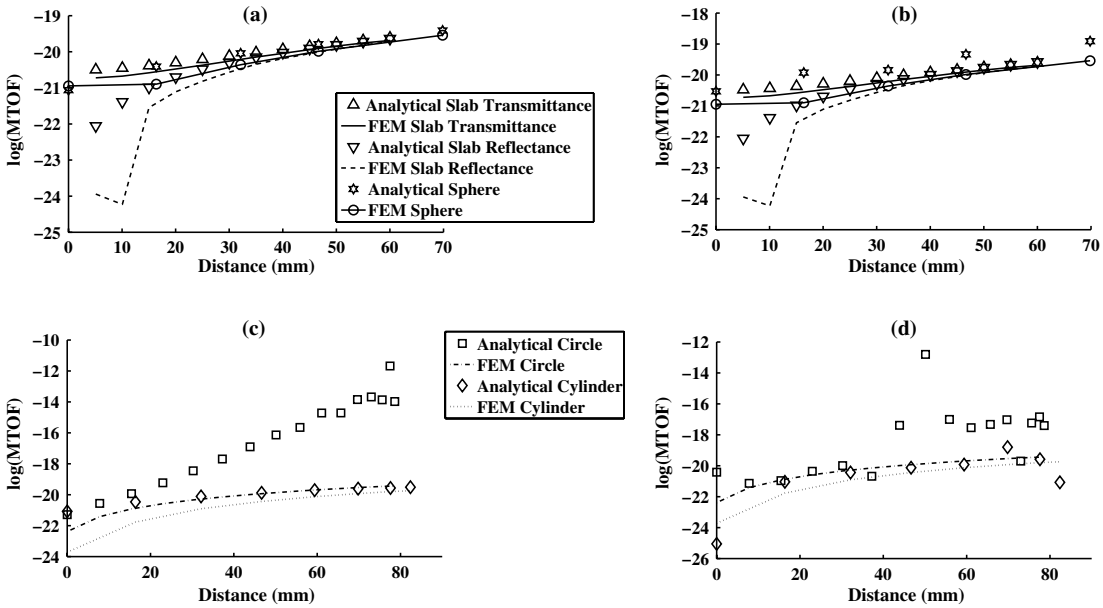

Fig. 4. (a) and (c) Same effort as Figs. 2(a) and 2(c) with ZBC in the case of analytical solution for the MTOF data. (b) and (d) Same effort as (a) and (c) except analytical solution is computed using EBC.

Table 3. Comparison of Computational Time Required for Computing Amplitude Using Numerical (FEM) and Analytical Models Using ZBC and EBC[a]

Geometry	FEM (ZBC)	Analytical (ZBC)	MTOF (ZBC)	MTOF (EBC)
Slab (Transmittance + Reflectance)	28.145729	0.001700	0.0191	0.0191
Circle	5.972411	4.253466	17.690	54.037
Cylinder	29.308491	8.445070	46.07	94.122
Sphere	41.751525	9.469508	14.07	26.51

[a]The last two columns give the MTOF computation time. The computation time is measured in seconds.

A. Note on Analytical Solutions Computation

The infinite sum in the analytical solution as given in Fig. 3 for the frequency domain in infinite slab case (Table 3 of [1]) has been truncated to the first fifty terms, as the accuracy of the solution does not improves much upon including further terms. The calculation of amplitude and MTOF involving infinite summation of term containing ratio of Bessel functions in Circular, Cylindrical, and Spherical geometries as given in Tables 9–10 of [1] have been continued until the values are nondegenerate, to subside the oscillatory nature of the Bessel functions when subjected to ZBC. However, in case of EBC, the infinite summations have been suitably truncated as the evaluation of expressions involving EBC are six times more computationally expensive. The outer summation running over odd roots of Bessel function for Cylindrical geometry (Table 5 of [1]) has been limited to a maximum of three roots for accurate approximation of the flux without resulting in any degenerate values during computation when subjected to ZBC. However, in case of EBC, the summation over roots of Bessel functions was increased to 9/11 as an upper threshold was put on number of terms to be included for the inner loops to reduce the computational complexity.

As all computations were performed as a function of the source–detector distance, an average value of the data having the same source–detector distance was used in here to remove the asymmetry in mesh discretization in the FEM-based solutions.

4. USAGE/EXTENSION OF GENERIC SOLUTION TO OTHER REGULAR GEOMETRIES

We discuss the usage/extension of the generic formulation of the Green's function solution (Eq. (53) of part I [1]) for any other regular geometry by writing down the analytical solution for cube. The discussion is limited to the time-domain case, as the frequency-domain solution could be written by taking Fourier transform. The cube geometry is as shown in Fig. 5(a). If the solution has to be derived from first principles, as discussed in the companion part [1] for other geometries, first it needs suitable rewriting of the infinite geometry solution and determining the coefficients for the general solution by making the sum total of the Green's function and the auxiliary solutions equal to zero on the boundaries. However, to demonstrate that Eq. (53) in [1] makes this task effortless, we make use of the Green's function solution for the rectangular parallelepiped available in [6], when subjected to change of origin to the center of the parallelepiped to satisfy the ZBC on $x = -a/2, x = a/2; y = -b/2, y = b/2; z = -c/2, z = c/2$ (a, b, c represents the length, breadth, and thickness of the rectangle) is given by

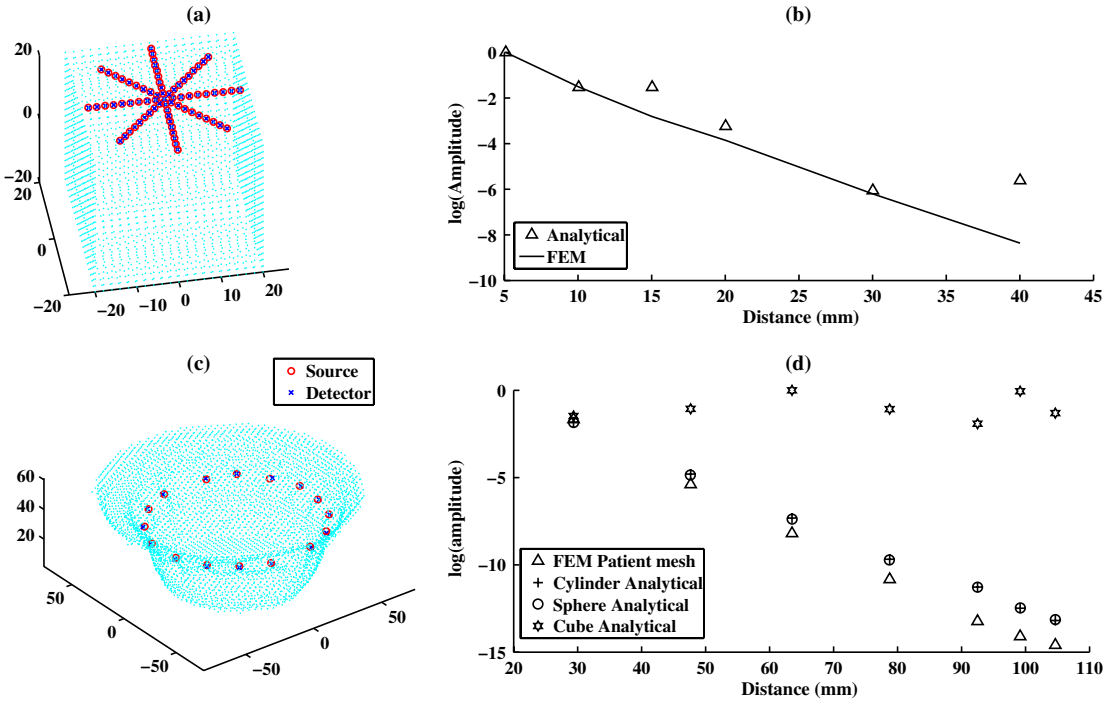

Fig. 5. (Color online) (a) Cube geometry showing the source/detector arrangement that was used for numerical solution (FEM) computation. (b) Comparison of analytical solution [Eq. (3)] and FEM solution as a function of source/detector distance. (c) Breast geometry that was used for generating numerical experimental data. (d) The comparison of computed data that were obtained using the best fits obtained using the analytical models (given in the legend).

$$g_{rp}^{\phi_p}(\mathbf{r},\mathbf{r}',t,t') = \frac{8}{abc}\sum_{l=1}^{\infty}\sum_{m=1}^{\infty}\sum_{n=1}^{\infty}\sin\frac{l\pi x}{a}\sin\frac{l\pi x_0}{a}\sin\frac{m\pi y}{b} \times\sin\frac{m\pi y_0}{b}\sin\frac{n\pi z}{c}\sin\frac{n\pi z_0}{c}e^{-\gamma_p^2\pi^2(t-t')\left[\frac{l^2}{a^2}+\frac{m^2}{b^2}+\frac{n^2}{c^2}\right]}, \tag{1}$$

where $\mathbf{r} = x\hat{i} + y\hat{j} + z\hat{k}$, $\mathbf{r}' = x_0\hat{i} + y_0\hat{j} + z_0\hat{k}$. Cube $a = b = c$ makes the above equation as

$$g_{\text{cube}}^{\phi_p}(\mathbf{r},\mathbf{r}',t,t') = \frac{8}{a^3}\sum_{l=1}^{\infty}\sum_{m=1}^{\infty}\sum_{n=1}^{\infty}\sin\frac{l\pi x}{a}\sin\frac{l\pi x_0}{a}\sin\frac{m\pi y}{a} \times\sin\frac{m\pi y_0}{a}\sin\frac{n\pi z}{a}\sin\frac{n\pi z_0}{a}e^{-\gamma_p^2\pi^2(t-t')\left[\frac{l^2+m^2+n^2}{a^2}\right]}. \tag{2}$$

So the generic solution by applying Eq. (53) in [1] is

$$g_{\text{cube}}^{\phi_{\text{fl}}}(\mathbf{r},\mathbf{r}',t,t') = \frac{n\zeta^2\gamma_m^2}{\gamma_m^2-\gamma_x^2}[g_{\text{cube}}^{\phi_x}(\mathbf{r},\mathbf{r}',t,t') - g_{\text{cube}}^{\phi_m}(\mathbf{r},\mathbf{r}',t,t')] * \left[\frac{1}{\tau-\zeta^2}[(e^{-\frac{t}{\tau}} - e^{-\frac{t}{\zeta^2}})u(t)]\right]. \tag{3}$$

The terms/symbols are defined in the companion paper [1]. The FEM solution is computed using cube geometry as shown in Fig. 5(a), with $a = 40$ mm. The details of the mesh are given in Table 1. The optical properties that were used for both analytical and numerical computations are same as the ones given in Table 2. The comparison of the logarithm of the amplitude data as a function of source detector distance is given in Fig. 5(b). Note that this analytical solution is computed with ZBC; even the general trends in the solutions are matching. The large discrepancy at the boundary of the imaging domain is primarily due to the boundary condition deployed. In the numerical solution, Type III was deployed and Type I was for the analytical solution.

5. EXTENSION OF THE DEVELOPED ANALYTICAL SOLUTIONS TO INHOMOGENEOUS MEDIUM AND IRREGULAR GEOMETRIES

Human tissue can be approximated with an inhomogeneous composite medium having homogeneous tissues layered on top of one another [7]. We may consider two discretization processes that have advantages in terms of computational complexity or numerical accuracy where the general form of the proposed solution holds true.

A. Case 1: Rectangular Discretization

We can consider any irregular geometry Ω surrounded by $\partial\Omega$ as the surface consisting of composite volumes of homogeneous medium [6]. We proceed by discretizing the volume into contiguous cuboids. Consider two adjacent cuboids surrounded by $x_0 \le x \le x_1$, $y_0 \le y \le y_1$, $z_0 \le z \le z_1$ and $x_1 \le x \le x_2$, $y_0 \le y \le y_1$, $z_0 \le z \le z_1$, respectively. Suppose the properties of the medium are in the region $x \le x_1$ are χ_0, $\Phi_{\text{fl}0}$, and for $x > x_1$, χ_2, $\Phi_{\text{fl}2}$. Within the voxels described, the medium is homogeneous and the analytical form of the coupled diffusion equations hold good; with care being taken to meet the boundary conditions at the plane of separation $x = x_1$ being

$$\Phi_{\text{fl}0} = \Phi_{\text{fl}2}, \quad x = x_1, \quad t > 0; \qquad \frac{\partial\Phi_{\text{fl}0}}{\partial x} = \frac{\partial\Phi_{\text{fl}2}}{\partial x}, \quad x = x_1, \quad t > 0,$$

where Φ_{fl2} is the flux in the region $x \geq x_1$, and Φ_{fl0} in the region $x \leq x_1$.

This procedure is independent of the nature of the medium and the geometry of consideration. The discretization has been considered with cuboids as it is convenient to calculate of $\hat{n}$, the unit normal perpendicular to the surface of separation. However such a scheme is an imitation of the finite difference scheme for solving differential equations and hence are limited by speed–accuracy tradeoff encountered when choosing the step length to be used for discretization.

B. Case 2: Contour Discretization

In this case of contour discretization, a concentric layered structure can be followed with the suitable geometry that approximates the tissue closely needs to be selected [6]. The assumption being that the volume Ω can be thus discretized into concentric layers separated by series of $\partial\Omega$ surfaces, where the tissue is homogeneous between any two boundaries. In general the equations for discretization should satisfy the following conditions:

$$\Phi_{fl0}|_{\partial\Omega} = \Phi_{fl2}|_{\partial\Omega}, \quad t > 0; \qquad \left.\frac{\partial\Phi_{fl0}}{\partial n}\right|_{\partial\Omega} = \left.\frac{\partial\Phi_{fl2}}{\partial n}\right|_{\partial\Omega}, \quad t > 0,$$

where Φ_{fl0}, Φ_{fl2} denote the flux on the inside and outside of the surface $\partial\Omega$.

However given the computational complexity (Table 3), such a discretization procedure will prove to be inefficient compared to FEM calculation for more than 4–8 layered discretization of the entire volume. A detailed description of the these methods as applied to heat diffusion equations can be found in [6].

6. DETERMINING BULK FLUORESCENCE PROPERTIES FROM EXPERIMENTAL DATA

One important usage of analytical solutions is its ability to determine the bulk fluorescence properties of the inhomogeneous and irregular media, such as breast. In here, we show such a usage via considering a breast mesh that is truly inhomogeneous, having typical breast tissue types, such as fatty, fibroglandular, and tumor. The breast mesh geometry along with source/detector positions are given in Fig. 5(c). The fatty tissue properties are same as in Table 2 except $\tau = 0.1$ ns, typically a large part of the breast. The fibroglandular region had the same properties as fatty tissue except for the region $\tau = 0.5$ ns and the tumor region, which occupies only 5% of the total volume, had a value of 0.8 ns. The rest of the properties were homogeneous in the breast volume. The source/detector arrangement was same as Dartmouth-NIR system [8] with 16 fibre optical bundles, when one acts as source rest act as detectors. The diameter of data-collection ring was 106 mm and the arrangement was given in Fig. 5(c). Note that only the continuous-wave case, where the data becomes the logarithm of amplitude, is considered in this case. The data obtained was plotted in Fig. 5(d).

Three geometries were considered to fit for the numerical experiment solutions, cylinder, sphere, and cube having diameter/thickness same as 106 mm. In case of cylinder, the height was considered as 60 mm. The same meshes that were specified in Table 1 were utilized by appropriately changing the dimensions, which also changes the nodal distance. For the same source/detector distance as considered in the numerical case, a series of values for τ starting from 0.001 to 1 ns in 1 ps was used. The ℓ_2-norm difference between the data vector values was considered as the metric for giving the best fit. For the cylinder, the homogeneous value of τ being 0.189 ns gave the best fit and the corresponding computed analytical solution is given in Fig. 5(d). The sphere homogenous value that gave the best fit was at 0.001 ns and for cube, it was 0.001 ns. All corresponding solutions are plotted in Fig. 5(d). As is evident from this exercise, the analytical solutions are capable of finding the bulk optical properties, if they are approximated by appropriate regular geometry (in here it is cylinder). If inappropriate regular geometry approximation is chosen, the bulk optical properties estimation might be erroneous, sometimes resulting in τ being 0.

7. CONCLUSIONS

In the first part of the work [1], we derived the analytical solutions along with the widely used data type for various regular geometries that are encountered in diffuse fluorescence imaging spectroscopy using both ZBCs and EBCs. In this part, we have validated these analytical solutions with the results obtained using established (finite element based) numerical models. The obtained results using analytical expressions and finite element based solutions were in close agreement for the frequency-domain case irrespective of the boundary condition deployed in analytical case. For the time-domain case, especially for calculation of MTOF, the EBC seems to be better suited, especially near the source, with a caveat that EBC analytical solutions are computationally complex compared to their counterpart. Note that this is also first time the solutions obtained by ZBCs and EBCs were compared in the same setup. The finite element models considered here were rather large in size (fine meshes with submillimeter nodal distances) to take care of numerical accuracy. Even though solutions for a couple of geometries were validated in here, the observed trend will be true for other geometries.

Moreover, an extension of the generic solutions that were derived in part I [1] for other geometries that were not discussed was shown via an example case of cube. Similarly, a discussion of usage of these analytical solutions for finding bulk optical properties was also performed through an example case, showing the utility of these solutions.

As fluorescence imaging is the biggest molecular imaging contender for small animal imaging [9], and most modern imaging systems involve usage of optical coupling medium between the animal and detector, making the imaging domain more regular [10], the solutions that were derived and validated here will have larger utility in these scenarios.

ACKNOWLEDGMENTS

This work is supported by the Department of Atomic Energy Young Scientist Research Award (No. 2010/20/34/6/BRNS) by the Government of India. The authors are grateful to anonymous reviewers, who gave the idea of using extrapolated boundary conditions as well as finding the bulk optical properties using analytical solutions, which improved the footage of the work presented here. The authors also thank the NIR imaging group of Dartmouth for providing the necessary patient meshes that were used in this work.

REFERENCES

1. K. R. Ayyalasomayajula and P. K. Yalavarthy, "Analytical solutions for diffuse fluorescence spectroscopy/imaging of biological tissues in regular geometries. Part I: zero and extrapolated boundary conditions," J. Opt. Soc. Am. A **30**, 537–552 (2013).
2. H. Dehghani, M. E. Eames, P. K. Yalavarthy, S. C. Davis, S. Srinivasan, C. M. Carpenter, B. W. Pogue, and K. D. Paulsen, "Near infrared optical tomography using NIRFAST: algorithms for numerical model and image reconstruction algorithms," Commun. Numer. Methods Eng. **25**, 711–732 (2009).
3. M. S. Patterson, B. Chance, and B. C. Wilson, "Time resolved reflectance and transmittance for the non-invasive measurement of tissue optical properties," Appl. Opt. **28**, 2331–2336 (1989).
4. M. Sadoqi, P. Riseborough, and S. Kumar, "Analytical models for time resolved fluorescence spectroscopy in tissues," Phys. Med. Biol. **46**, 2725–2743 (2001).
5. S. L. Jacques and B. W. Pogue, "Tutorial on diffuse light transport," J. Biomed. Opt. **13**, 041302 (2008).
6. H. S. Carslaw and J. C. Jaeger, *Conduction of Heat in Solids*, 2nd ed. (Oxford Science, 1946).
7. C. K. Hayakawa, J. Spanier, F. Bevilacqua, A. K. Dunn, J. S. You, B. J. Tromberg, and V. Venugopalan, "Perturbation Monte Carlo methods to solve inverse photon migration problems in heterogeneous tissues" Opt. Lett. **26**, 1335–1337 (2001).
8. T. O. McBride, B. W. Pogue, S. Jiang, U. L. Osterberg, and K. D. Paulsen, "A parallel-detection frequency-domain near-infrared tomography system for hemoglobin imaging of the breast in vivo," Rev. Sci. Instrum. **72**, 1817–1824 (2001).
9. E. M. Sevick-Muraca and J. C. Rasmussen, "Molecular imaging with optics: primer and case for near-infrared fluorescence techniques in personalized medicine," J. Biomed. Opt. **13**, 041303 (2008).
10. S. Patwardhan, S. Bloch, S. Achilefu, and J. Culver, "Time-dependent whole-body fluorescence tomography of probe bio-distributions in mice," Opt. Express **13**, 2564–2577 (2005).